PLASMA PHYSICS

A. BOUCHIKHI

University of Saïda, Faculty of technology, Department of electrical engineering
(Saïda 20000, Algeria)

STUDY OF THE NEON DIELECTRIC BARRIER DISCHARGE ON A CAPACITIVELY COUPLED RADIO FREQUENCY AT A LOW PRESSURE WITH METASTABLE ATOM DENSITY: EFFECT OF THE PRESSURE

We study the neon dielectric barrier discharge with metastable atom density on a capacitively coupled radio frequency at a pressure of about 4–12 Torr. The transport parameters of neon are dependent on the electron energy, and their range is about 0.04–50 eV. A one-dimensional fluid model and the drift-diffusion theory are used to describe the neon dielectric barrier discharge. The effect of the gas pressure on the properties of neon dielectric barrier discharge is presented for the cycle-averaged regime. It is shown that the particle densities, electric potential, and metastable atom density increase with the pressure. In addition, the surface charge concentration and the gap voltage increase as well.

K e y w o r d s: capacitively coupled, RF glow discharge, Gauss law, dielectric barrier discharges.

1. Introduction

Glow discharge plasma [1–11] produced by a powered DC or a RF source has various applications in industrial technologies and medical therapy. Among which, an improved discharge by the substance vapor deposition, a surface adaptation by different materials and the plasma etching. Furthermore, a capacitive geometry can enhance these technologies [12]. The last work presents a progressive technique to control the discharge by means of a dielectric barrier [13–16] at low or high pressures of the gas. In the medical domain, we find the dermatology treatment by means of coherent and incoherent ultraviolet (UV) and vacuum ultraviolet (VUV) radiations from a glow source.

Beside the experimental tools [17], the mathematical model is the best approach to describe and to optimize the discharge behavior mostly at the sides of electrodes and in the bulk plasma. Samir *et al.* [18]

have investigated the effect of a gas pressure on the capacitively coupled radio frequency (CCRF) in discharges in the argon gas. Thus, the electric potential increases, and the electron temperature decreases with increasing gas pressure. Liu *et al.* [19] have studied the effect of secondary electron emission coefficient (SEEC) on the capacitively coupled RF (CCRF) from argon glow discharges. They have demonstrated that increasing SEEC changes consequently many parameters such as the net power absorption, electron power dissipation, and thermal conductive term. Becker *et al.* [20] have presented a comparative study between argon and helium CCRF discharges by means of the advanced fluid model and particle-in-cell/Monte Carlo code.

Barjasteh and Eslami [21] have described the behavior of a discharge in DBDs at a low-pressure for gas mixtures (90%Ar–10%Cl$_2$). They have shown that the electronegativity property and the radiation process grow, when the voltage amplitude increa-

ses. However, when the frequency increases, the electronegativity property decreases. Barjasteh *et al.* [22] have studied the effect of the voltage parameters on the characteristics of the dielectric barrier discharge (DBD) in a low-pressure argon gas. It has been shown that increases in the applied voltage and voltage frequency lead to a growth in both the radiation process within the plasma and the discharge current.

In this work, we have interested to give a detailed description for the behavior of a neon glow discharge operated in CCRF and controlled by the dielectric barrier in the presence of a metastable atom density. Moreover, we will consider the gas pressure effect on the plasma characteristics.

2. Physical Model and Boundary Condition

A description of the adopted discharge scheme is depicted in Fig. 1. As we assume that the electrode size is greater than the interelectrode spacing, then the model has been computed in a one-dimensional geometry. The frequency of the RF power supply is set to 13.56 MHz, and the neon gas pressure is of about 4–12 Torr. Therefore, the RF driving frequency is less than the momentum transfer collision frequency. Consequentially, the fluid model is utilized to simulate the RF neon plasma.

In order to get a complete explanation of properties of the low-pressure neon plasma, both neon atoms and ions, as well as excited atoms, have been taken into account. The kinetic scheme of processes includes five electron collision reactions: the ionization in elastic collisions, excitation, deexcitation, and stepwise ionization related to the rate coefficients depending on the mean electron energy. Theses reactions are labelled as follows: P_{ec}, k_{io}, k_{ex}, K_{dex} and K_{io}^m, respectively. In addition, the chemo-ionization (K_{ci}) [23] and radiation processes (τ_m) [24] are considered. Table 1 summarizes these reactions and the relevant references. The processes k_{io}, k_{ex}, and K_{dex} are calculated using BOLSIG+ software [25–26], and the process K_{io}^m is determined according to the expression given by Vriens and Smeets [27].

Then, the model [6, 7] is described as follows:

$$\frac{\partial n_e}{\partial t} + \frac{\partial \Gamma_e}{\partial x} = S_e, \tag{1}$$

$$\frac{\partial n_+}{\partial t} + \frac{\partial \Gamma_+}{\partial x} = S_+, \tag{2}$$
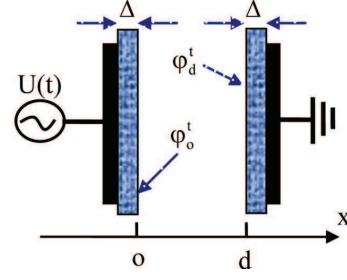

Fig. 1. Discharge configuration, φ_x^t is the electric potential at the dielectric side

$$\frac{\partial n_m}{\partial t} + \frac{\partial \Gamma_m}{\partial x} = S_m, \tag{3}$$

$$\frac{\partial \varepsilon_e n_e}{\partial t} + \frac{\partial \Gamma_{e\varepsilon}}{\partial x} = S_{e\varepsilon}, \tag{4}$$

$$S_e = S_+ = n_e n_g K_{io} + n_e n_m K_{io}^m + n_m n_m K_{ci}, \tag{5}$$

$$S_m = n_e n_g K_{ex} - n_e n_m K_{dex} - \\ - n_e n_m K_{io}^m - 2 n_m n_m K_{ci} - \frac{n_m}{\tau_m}, \tag{6}$$

$$\Gamma_e = -n_e \mu_e E - \frac{\partial D_e n_e}{\partial x}, \tag{7}$$

$$\Gamma_+ = n_+ \mu_+ E - \frac{\partial D_+ n_+}{\partial x}, \tag{8}$$

$$\Gamma_m = -D_m \frac{\partial n_m}{\partial x}, \tag{9}$$

$$\Gamma_{e\varepsilon} = -n_e \mu_{e\varepsilon} E - \frac{\partial D_{e\varepsilon} n_e}{\partial x}, \tag{10}$$

$$S_{e\varepsilon} = -e\Gamma_e E + \varepsilon_m n_e n_m K_{dex} + \varepsilon_{ci} n_m n_m K_{ci} - \\ - n_e P_{ec} - \varepsilon_m n_e n_g K_{ex} - \varepsilon_{io} n_e n_g K_{io} - (\varepsilon_{io} - \\ - \varepsilon_m) n_e n_m K_{io}^m, \tag{11}$$

$$\frac{\partial^2 \phi}{\partial x^2} = -\frac{e_o}{\varepsilon_o}(n_+ - n_e). \tag{12}$$

The synonyms of the difference notations utilized in the above equations are mentioned in Table 2 and represent the diffusion coefficient and mobility of the electron energy.

2.1. Boundary conditions

In this subsection, we will present the initial and boundary conditions. There are a lot of boundary conditions given by different expressions (see, e.g., Samir *et al.* [18] and Liu *et al.* [19]). Those boundary conditions read: The ion flux and electron temperature at each of the electrodes are given as follow: $\Gamma_+ = n_+ \mu_+ E$ and $T_e = 0.5$ eV.

Table 1. **Kinetic scheme of processes and their rate coefficients**

N	Processes	Rate coefficients	Refs.
P_1	$Ne + e^- \rightarrow Ne + e^-$	P_{ec} (eV s^{-1})	28
P_2	$Ne + e^- \rightarrow Ne^+ + 2e^-$	k_{io} (cm^3 s^{-1})	25–26
P_3	$Ne + e^- \rightarrow Ne_m^* + e^-$	k_{ex} (cm^3 s^{-1})	25–26
P_4	$Ne_m^* + e^- \rightarrow Ne + e^-$	K_{dex} (cm^3 s^{-1})	25–26
P_5	$Ne_m^* + Ne_m^* \rightarrow Ne^+ + e^- + Ne$	$K_{ci} = 3.6 \times 10^{-10}$ (cm^6 s^{-1})	23
P_6	$Ne_m^* \rightarrow Ne + h\nu$	$\tau_m = 2 \times 10^{-3}/p$ (s) and p in Torr	24
P_7	$e^- + Ne_m^* \rightarrow Ne^+ + 2e^-$	K_{io}^m (cm^3 s^{-1})	27

Table 2. **Description of the different notations utilized in our model**

Notations	Description
n_s	The particle density
S	Subscript
ε_e	The mean electron energy
Γ_s	The particle flux
ϕ	The electrostatic potential
$+$; e ; m	The positive ions; electrons; metastable atoms
n_g	The neutral gas density
S_e	The electron source term
$\phi_{e\varepsilon}$	The electron energy flux
$\mu_{e\varepsilon}$	The mobility of electron energy
$D_{e\varepsilon}$	The diffusion coefficient of electron energy
D_s	The diffusion coefficient of spieces (s)
E	The electric field
ε_o	The free space permittivity
e_o	The elementary charge
μ_s	The mobility of spieces (s)
$\Gamma_{e\varepsilon}$	The electron energy flux
$S_{e\varepsilon}$	The electron energy source term

At the ground electrode $(x = d)$: $\Gamma_e = -n_e K_s - \gamma\Gamma_+$.

The discharge reactor is powered at $(x = 0)$ by the sinusoidal voltage $U(t) = U_a \sin(2\pi f t)$. At the ground electrode $(x = d)$, $U(t) = 0$.

The initial densities are chosen in the Gaussian form; $n_e = n_+ = 10^7 + 10^9(1 - x/d)^2(x/d)^2$ cm^{-3} [29–30].

Other boundary conditions are cited per Hagelaar *et al.* [31] as follows:

The particle fluxes of electron and ions are written as

$$\Gamma_+ \cdot \nu = \frac{1 - r_+}{1 + r_+}\left(|n_+\mu_+ E| + \frac{v_+^{th} n_+}{2}\right), \quad (13)$$

Table 3. **Dielectric parameters and their references**

Dielectric parameters		Value	Refs.
Thickness		$\Delta = 1$ mm	
Reflection coefficient of electrons	Metallic	$r_e = 3 \times 10^{-1}$	32
	Dielectric	$r_e = 7 \times 10^{-1}$	32
Reflection coefficient of ions	Metallic	$r_+ = 5 \times 10^{-4}$	32
	Dielectric	$r_+ = 5 \times 10^{-3}$	32
Relative permittivity of dielectric	Borofloat glass	$\varepsilon_r = 4.6$	13
	Alumina	$\varepsilon_r = 10$	13

$$\Gamma_e \cdot \nu = \frac{1 - r_e}{1 + r_e}\left(|n_e\mu_e E| + \frac{v_e^{th} n_e}{2}\right) -$$
$$- \frac{2}{1 + r_e}\gamma\max(\Gamma_+ \cdot \nu), \quad (14)$$

where ν is equal to –1 at $(x = 0)$, and $\nu = 1$ at $x = d$, and $r_{e,+}$ is the reflection coefficient of electrons or ions, and their values are given in Table 3.

The thermal velocity of electrons or ions is given by:

$$v_{e,+}^{th} = \sqrt{\frac{8k_b T_{e,+}}{\pi m_{e,+}}}. \quad (15)$$

The Gauss law [13] is applied in the presence of the dielectrics, to compute the accumulation of surface charges on the dielectrics as follow:

$$\varepsilon_r\varepsilon_o E_{diel}(x, t) \cdot \nu - \varepsilon_o E(x, t) \cdot \nu = \sigma_s(x, t), \quad (16)$$

where $E_{diel}(x, t)$ is the electric field inside the dielectrics, and ε_r is their relative permittivity (see Table 3), and $E(x, t)$ is the electric field related to the gas discharge. To compute the electric potential at the dielectrics (φ_0^t and φ_d^t), we have em-

ployed Eq. (16). The temporal evolution of the surface charge density ($\sigma_s(x,t)$) begins from the breakthrough of the dielectrics by particle currents. This density is expressed by Becker *et al.* [17] as

$$\frac{\partial \sigma_s(x,t)}{\partial t} = e_o \sum_j \Gamma_j(x,t) \cdot \nu. \qquad (17)$$

The system of partial differential equations is discretized using the finite-difference method. Moreover, the equations of transport of particles and the energy have been discretized according to the exponential scheme [33–35]. The Poisson's equation has been discretized spatially by the central difference technique. Both steps in time and within space grids are uniform and constant. The number of grid points in space is equal to 250 and, per period time, is equal to (4×10^3). The neon transport parameters are given in Table 4.

3. Results and Discussion

3.1. With and without metastable atom density

In order to examine the effect of the metastable atom density on the discharge behavior, we have plotted the electrical characteristics with and without metastable atom density. Figure 2 shows the electron density profiles with and without metastable atom density. As we can see, the electron density with metastable atom density is higher than that without metastable atom density. This is due to the contribution of the stepwise ionization and chemoionization processes. We note that the maximum electron density with metastable atom density reaches 1.56×10^{10} cm^{-3}, and the maximum of the electron density without metastable atom density is equal to 1.38×10^{10} cm^{-3}. The total current with metastable atom density reaches –2.7 mA/cm^2, and it is equal to –2.6 mA/cm^2, when the metastable atom density is neglected.

3.2. With and without dielectrics

In order to examine the effect of the dielectric barrier, we have plotted both electric potential and electron temperature with and without dielectrics in Fig. 3. We can see that the electric potential with dielectrics is superior to that without dielectrics. We can explain this fact by that, without dielectrics, the electric potentials at both electrodes are constant and
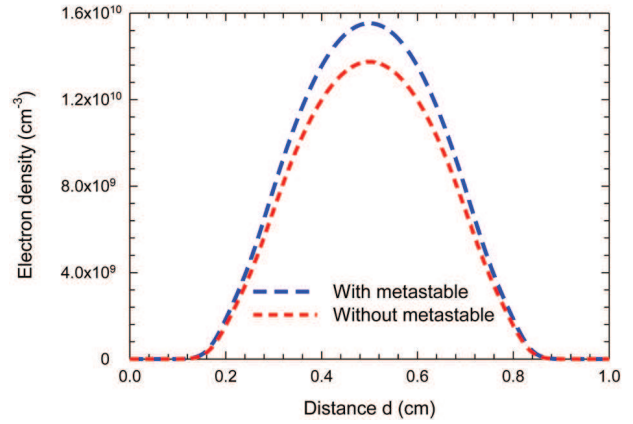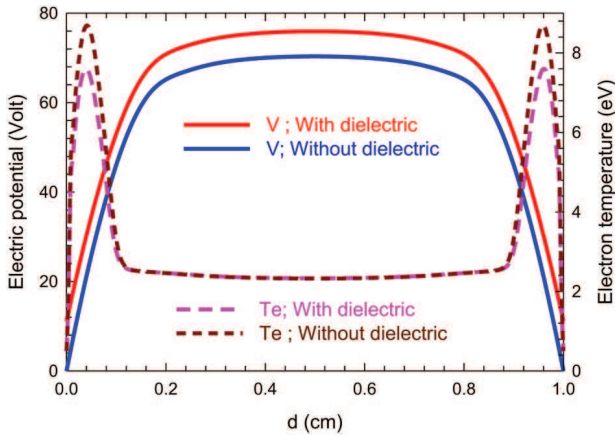

Fig. 2. Electron density profiles with and without metastable atom density at the 2000-th cycle CCRF neon dielectric barrier discharge, and those profiles are provided in the cycle-averaged regime

Table 4. **Discharge configuration and neon physical characteristics applied in a CCRF dielectric barrier discharge, E/n_g in Td**

Symbol	Definition	Value	Refs.
d	Electrode distance	1 (cm)	–
T_{gas}	Gas temperature	300 (K)	–
p	Pressure	4, 8, and 12 (Torr)	–
U_a	Voltage amplitude	150 (Volt)	–
f	Frequency	13.56 (MHz)	–
$n_g \mu_e$	Electron mobility	BOLSIG+	25–26
$n_g D_e$	Electron diffusion coefficient	BOLSIG+	25–26
W	Ion drift velocity	$\frac{11.27 E/n_g}{(1+0.01288 E/n_g)^{0.5}}$	36
D_+	Ion diffusion coefficient	$D_+ = \frac{\mu_+ T_{\text{gas}} K_{\text{B}}}{e_o}$	–
K_s	Electron recombination coefficient	$1.19 \times 10^7 (\text{cm s}^{-1})$	19
γ	Electron emission coefficient	0.04	–

are equal to the applied potential, i.e., 0 V at the ground electrode ($x = d$), and $U(t) = U_a \sin(2\pi ft)$ at the powered electrode ($x = 0$). Hence, these values are increased in the presence of the dielectrics by means of the Gauss law.

Figure 4 shows the profile of electron density and electric field with and without dielectrics. We can see that the electron density without dielectrics is superior to that with dielectrics. Therefore, the electric field without dielectrics is superior to that with di-
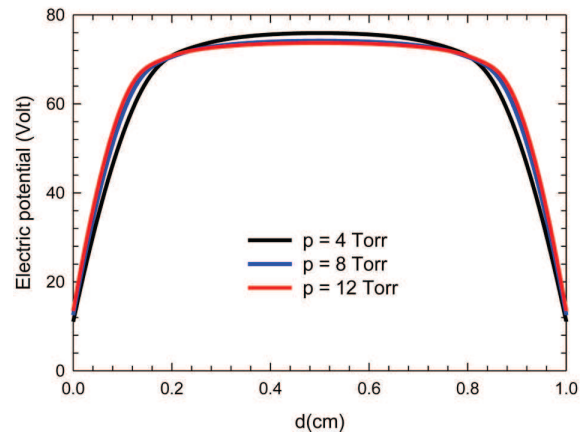
Fig. 3. Electric potential and electron temperature profiles with and without dielectrics at the 2000-th cycle CCRF neon dielectric barrier discharge, and those profiles are provided in the cycle-averaged regime
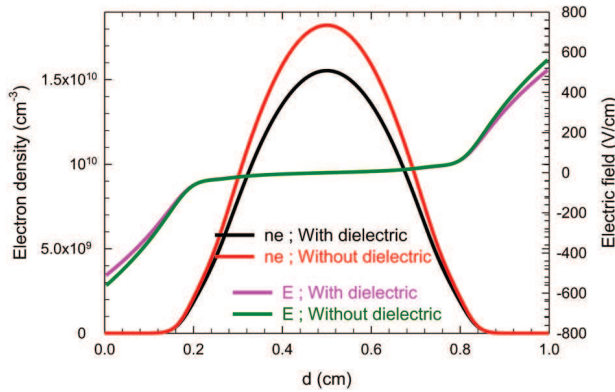
Fig. 4. Electron density and electric field profiles with and without dielectrics at the 2000-th cycle CCRF neon dielectric barrier discharge, and those profiles are provided in the cycle-averaged regime

electrics (see Fig. 4). Consequently, the electron temperature without dielectrics is superior to that with dielectrics (see Fig. 3).

Figure 5 shows the profiles of the electric potential as a function of the pressure at the 2000-th cycle CCRF neon dielectric barrier discharge. Those profiles are given within the cycle-averaged regime. We remark that the width of the plasma region increases with the pressure. We can explain this fact by the magnification of the pressure, the neutral gas density growth, and then the collision processes increase, i.e., the ionization, stepwise ionization, and chemoionization rise as well. These processes do to raise parti-

Fig. 5. Electric potential profiles as a function of the pressure at the 2000-th cycle CCRF neon dielectric barrier discharge, and those profiles are provided in the cycle-averaged regime

cle densities (electron and ion ones). On the other hand, With gas pressure growing, there is a decrease of the electron displacement amplitude in the RF electric field in plasma, and the smaller this electron displacement amplitude, the thinner the sheaths and the broader the plasma region. Consequently, the length of the electric potential increases with the pressure. We note that the maxima of the electric potential are equal to 75.93, 74.20, and 73.71 V, when the gas pressure is equal to 4, 8, and 12 Torr, respectively. The behavior of the electric potential is characterized by two sheath thicknesses, between which a bulk plasma region is located. This behavior is again characterized by the maximum and minimum values of the potential. Then, the landing potential is computed as the difference between the maximum and the minimum values of the electric potential. Thereby, the landing potential is equal to 64.85, 61.63, and 60.24 V, when the pressure is equal to 4, 8, and 12 Torr, respectively. We remark that the landing potential decreases, as the pressure increases.

Figure 6 represents the curve of the metastable atom density as a function of the pressure at the 2000-th cycle CCRF neon dielectric barrier discharge. This picture provides the cycle-averaged regime. We remark that the metastable atom density has a Gaussian form, and their maximum is located at the middle of the interelectrode spacing. We see that the metastable atom density decreases, as the pressure increases. This is due to the diminution of the radiation

508

process and the diffusion coefficient of the metastable atom density. It is obvious that the maximum of the metastable atom density changes from (3.07×10^{11}) to (1.90×10^{11}) cm^{-3}, when the pressure changes from 4 to 12 Torr.

Figure 7 shows the profiles of the electron temperature as a function of the pressure at the 2000-th cycle of a CCRF neon dielectric barrier discharge, and these profiles are presented in the cycle-averaged regime. As one can see, the profile of the electron temperature has two peaks. This distribution is caused by plasma electrons in the anode phase that fill the near-electrode layer (when the corresponding electrode possesses the instantaneous positive potential). In the cathode phase, the electrons are swept out of the layer back into plasma. As a result, they acquire the energy with the appearance of peaks on the electron temperature plot near the boundaries of the layers [37–38]. On the contrary, the cooling phenomenon created by means of the electron density and the ground state of neon atoms, as well as the threshold ionization and excitation are weakening in the sheath thickness. In the bulk plasma region, the cooling phenomenon is greater due to the presence of a high electron density. We remark that the electron temperature decreases with the increasing of the pressure; this is due to the diminution of the mean free path, and this latter serves to diminish the electron energy. As a result, the electron temperatures diminish in both the sheath and in the bulk plasma.

It is obvious that the electron temperature changes from 7.60 to 6.35 eV in the sheath and alters from 2.33 to 1.75 eV in the bulk plasma, when the pressure varies from 4 to 12 Torr.

In order to show the behavior of discharges, we give the summary of studies of the plasma density and the electric field as functions of the pressure at the 2000-th cycle averaged in CCRF neon dielectric barrier discharge in Table 5. As one can see that the plasma density increases with the pressure from (1.55×10^{10}) to (5.53×10^{10}) cm^{-3}. This is due to that the augmentation of the pressure serves to augment the gas density. Then, the particle densities are increased. As a consequence, the electric field increases with the pressure from 509.88 to 619.80 V/cm.

In order to valid our numeric code, we have investigated our discharges without dielectrics and in comparing our results and those obtained by Samir *et al.* [18], Park and Economou [39], Meyyappan
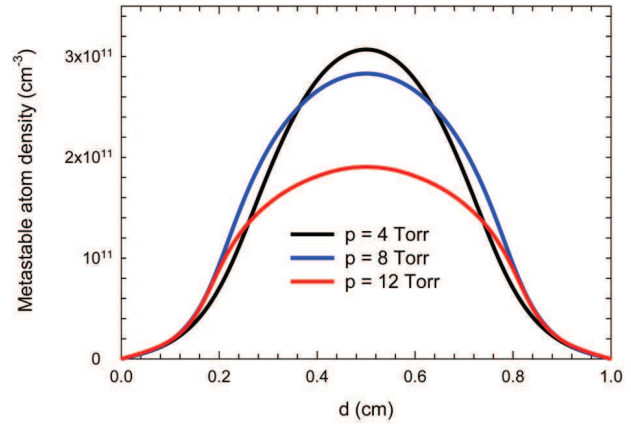

Fig. 6. Metastable atom density curves as a function of the pressure at the 2000-th cycle CCRF neon dielectric barrier discharge. This picture provides the cycle-averaged regime
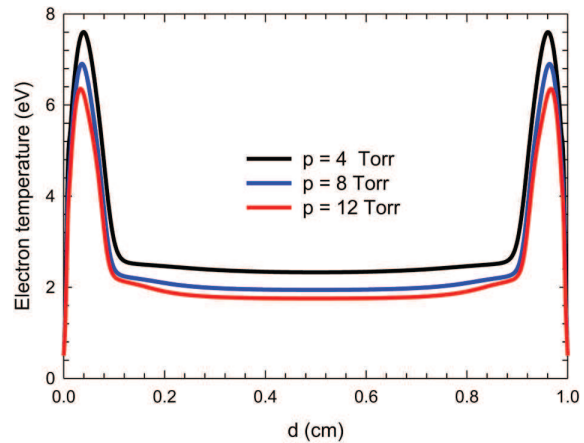

Fig. 7. Electron temperature profiles depend on the pressure at the 2000-th cycle CCRF neon dielectric barrier discharge, and these profiles are provided in the cycle-averaged regime

Table 5. **Summary of the plasma density and the electric field as a function of the pressure at the 2000-th cycle averaged in a CCRF neon dielectric barrier discharge**

Pressure (Torr)	Plasma density (cm^{-3})	Electric field (V/cm)
4	1.55×10^{10}	509.88
8	3.63×10^{10}	577.92
12	5.53×10^{10}	619.80

and Govindan [40], Hwang *et al.* [41], Surendra and Vender [42], and Surendra *et al.* [43]. We have found a reasonable agreement.
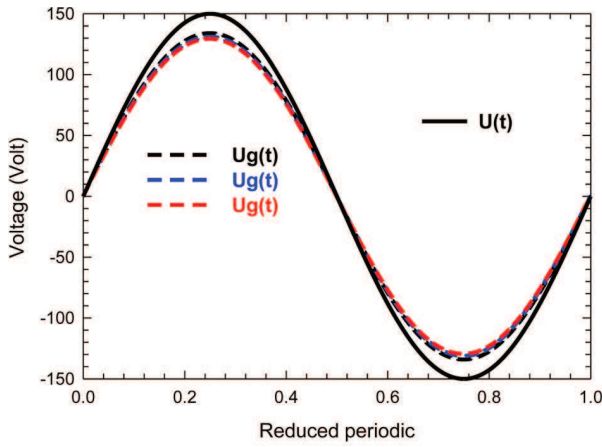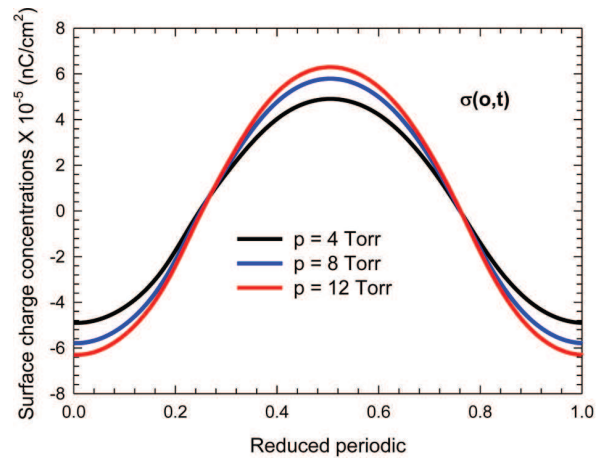
Fig. 8. Effect of the pressure on the gap voltages as a function of the reduced periodicity of a CCRF neon dielectric barrier discharge at the 2000th cycle, and $U(t)$ is the applied voltage
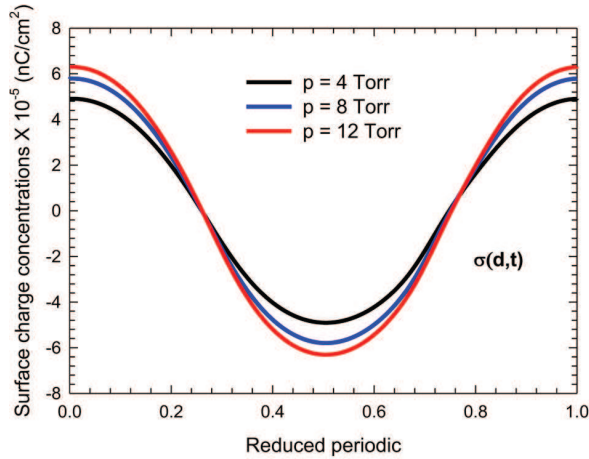
Fig. 9. Effect of the pressure on the surface charge concentration $\sigma_s(d,t)$ as a function of the reduced periodicity of a CCRF neon dielectric barrier discharge at the 2000th cycle

Figure 8 represents the effect of the pressure on the gap voltages as functions of the reduced periodicity of a CCRF neon dielectric barrier discharge at the 2000th cycle. To examine this effect, we have plotted the applied voltage $(U(t))$. We have defined the gap voltage $(U_g(t))$ as: $(U_g(t) = \phi_0^t - \phi_d^t)$. As a consequence, the gap voltage is inferior to the applied voltage. It is worth noting that the resulting form of the gap voltage is sinusoidal. This is due to the source voltage which has a sinusoidal form. Note that the amplitude of the gap voltage is decreased to 134.05, 131.10, and 129.43 V for the gas pressures equal to 4, 8, and 12 Torr, respectively.
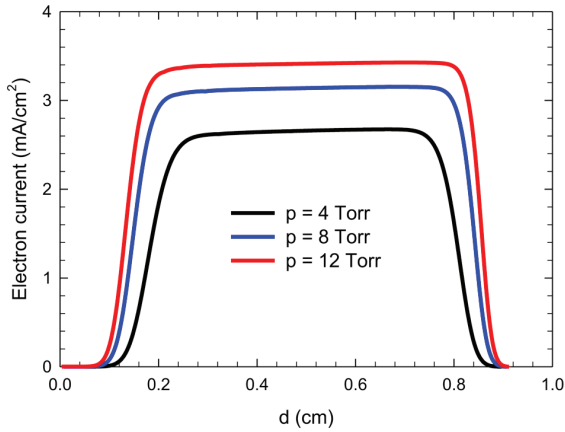

Fig. 10. Effect of the pressure on the surface charge concentration $\sigma_s(o,t)$ as a function of the reduced periodicity of a CCRF neon dielectric barrier discharge at the 2000th cycle

As a result, the difference voltage between the applied voltage and the gap voltage is of about 15.95, 18.9, and 20.57 V. We remark that the difference in voltages increases with the pressure.

Figure 9 shows the effect of the pressure on the surface charge concentration $(\sigma_s(d,t))$ as a function of the reduced periodicity of a CCRF neon dielectric barrier discharge at the 2000th cycle. The morphology of the surface charge concentration $(\sigma_s(d,t))$ strictly follows the gap voltage structure. The surface concentrations reflect the precipitation of particles charged on the dielectrics, and this precipitation increases in time. As one can see, the surface concentration $(\sigma_s(d,t))$ increases with the pressure, and the maximum changes from 4.91×10^{-5} to 6.3×10^{-5} nC/cm^2, when the pressure changes from 4 to 12 Torr. This is due to the augmentation of the electric field at the electrodes.

Figure 10 shows the effect of the pressure on the surface charge concentration $(\sigma_s(o,t))$ as a function of the reduced periodicity of a CCRF neon dielectric barrier discharge at the 2000th cycle. As one can see, the morphology of the surface charge concentration $(\sigma_s(o,t))$ has the same behavior as $(\sigma_s(d,t))$, and they have the reversed polarities, i.e., while the surface charge concentration $(\sigma_s(d,t))$ has a maximum value, $(\sigma_s(o,t))$ has a minimum value, and vice versa, as well as this morphology is conserved at each period. The effect of the pressure on the surface charge concentration $(\sigma_s(o,t))$ is similar to that of $(\sigma_s(d,t))$, and the amplitude of $(\sigma_s(o,t))$ changes from 4.91×10^{-5}
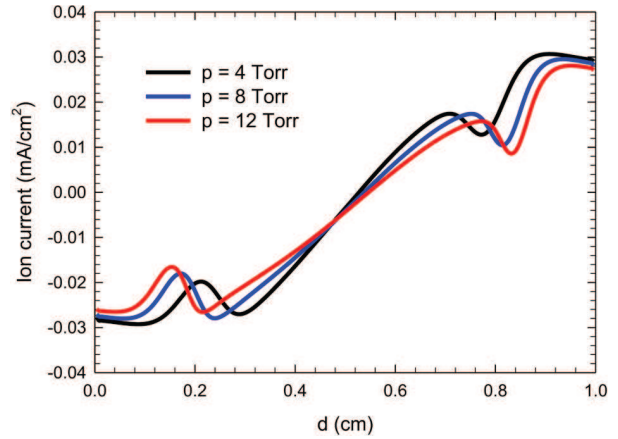
Fig. 11. Effect of the pressure on the electron current at the 2000-th cycle of a CCRF neon dielectric barrier discharge at the phase $wt = \pi$

Fig. 12. Effect of the pressure on the ion current at the 2000-th cycle pf a CCRF neon dielectric barrier discharge at the phase $wt = \pi$

Fig. 13. Effect of the pressure on the displacement current at the 2000-th cycle of a CCRF neon dielectric barrier discharge at the phase $wt = \pi$

to 6.3×10^{-5} nC/cm^2, when the pressure changes from 4 to 12 Torr, as well as this augmentation is due to the augmentation of the electric field at the electrodes.
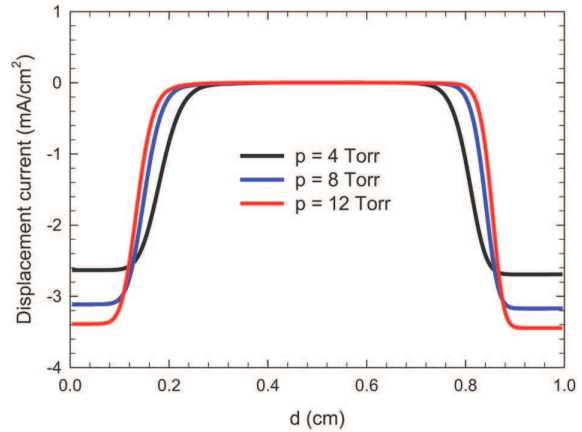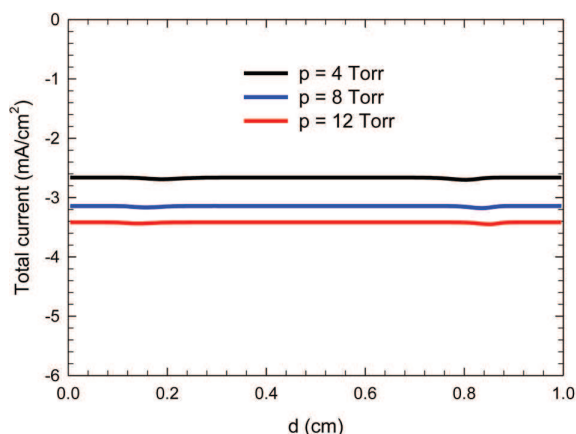
Figure 11 shows the effect of the pressure on the electron current at the 2000-th cycle of a CCRF neon dielectric barrier discharge at the phase ($wt = \pi$). We remark that the electron current is characterized by two sheath thicknesses located at both electrodes and plasma region. As one can see, the effect of the pressure is independent of both sheath thicknesses, but in the plasma region and the electron current increase with the pressure because of the augmentation of the electron density. We remark that the electron current is quasiconstant in the plasma region.

We note that the maxima of the electron current are 2.67, 3.15, and 3.43 mA/cm^2 by means of the effect of the pressure equal to 4, 8, and 12 Torr, respectively.

Figure 12 shows the effect of the pressure on the ion current at the 2000-th cycle of a CCRF neon dielectric barrier discharge at the phase ($wt = \pi$). We remark that the spatial distribution of the ion current is symmetric compared at the middle of the interelectrode spacing. This situation is due to the electric field behavior on the ion current. As one can see, the ion current decreases with the augmentation of the pressure due to the expansion of the plasma region. It is obvious that the maximum of the ion current changes from 0.03 to 0.03 mA/cm^2, when the pressure changes from 4 to 12 Torr.

Figure 13 shows the effect of the pressure on the displacement current at the 2000-th cycle of a CCRF neon dielectric barrier discharge at the phase ($wt = = \pi$). We remark that the spatial distribution of the displacement current is characterized by two sheath thicknesses placed beside at both electrodes; between them, a plasma region is located. As one can observe, the behavior of the displacement current is inversely related to that of the electron current. The effect of the pressure on the displacement current in the plasma region is independent, i.e., regardless of the pressure, the displacement current does not change. Beside that, the displacement current in-

Fig. 14. Effect of the pressure on total current at the 2000-th cycle of a CCRF neon dielectric barrier discharge at the phase $wt = \pi$

creases with the pressure. It is obvious that the maxima of the displacement current are placed at 2.7, 3.2, and 3.45 mA/cm² by means of the effect of the pressure equal to 4, 8, and 12 Torr, respectively. In the plasma region, the displacement current is null regardless of the pressure.

Figure 14 shows the effect of the pressure on the total current at the 2000-th cycle of a CCRF neon dielectric barrier discharge at the phase ($wt = \pi$). The total current represents the sum of the electron, ion, and metastable atoms, as well as the displacement currents. Other than that, the current of metastable atoms is negligible, and it is not shown. As a consequence, the fall of both electron and displacement currents is faded away between them, and the total current is constant in the interelectrode spacing. It is obvious that the total current is –2.7, –3.15 and –3.42 mA/cm² by means of the effect of the pressure equal to 4, 8, and 12 Torr, respectively, at the phase ($wt = \pi$).

4. Conclusion

Three moments of Boltzmann's equation with Poisson's equation are taken to describe a capacitively coupled neon glow discharge driven by the radio frequency power at low pressures with dielectrics, and the metastable atom density is introduced again in the model. Mainly to describe the model, we have used the expression for a particle flux that can explain the kinetics of electrons and ions by the Gauss law, as well as the accumulation of charged particles

on the dielectrics. The effect of boundary conditions in the presence of a dielectrics is well defined from the spatial distribution of the surface charge concentrations and the gap voltage temporally. The effect of the pressure on the discharge characteristics is presented on the cycle-averaged plots. As a result, the particle densities, electric field, and electric potential increase with the pressure. In addition, the surface charge concentration and the gap voltage increase again. The electron temperature decreases with the augmentation of the pressure.

1. T. Samir, Y. Liu, L.-L. Zhao, Y.-W. Zhou. Effect of driving frequency on electron heating in capacitively coupled RF argon glow discharges at low pressure. *Chin. Phys. B* **26**, 115201 (2017).
2. L.-L. Zhao, Y. Liu, T. Samir. Effects of gas pressure on plasma characteristics in dual frequency argon capacitive glow discharges at low pressure by a self-consistent fluid model. *Chin. Phys. B* **26**, 125201 (2017).
3. M. Meyyappan, J.P.L. Kreskovsky. Glow discharge simulation through solutions to the moments of the Boltzmann transport equation. *J. Appl. Phys.* **68**, 1506 (1990).
4. B. Hechelef, A. Bouchikhi. Current–voltage characteristics in a helium–argon gas mixture glow discharge at low pressure. *Acta Physica Polonica A* **136**, 855 (2019).
5. M.M. Becker, D. Loffhagen. Enhanced reliability of drift-diffusion approximation for electrons in fluid models for nonthermal plasmas. *AIP Advances* **3**, 012108 (2013).
6. T. Alili, A. Bouchikhi, M. Rizouga. Investigations of argon and neon abnormal glow discharges in the presence of metastable atom density with fluid model. *Can. J. Phys.* **94**, 731 (2016).
7. M.M. Becker, D. Loffhagen W. Schmidt. A stabilized Finite Element Method for Modeling of gas Discharges. *Comp. Phys. Com.* **180**, 1230 (2009).
8. B. Hechelef, A. Bouchikhi. Identification of the normal and abnormal glow discharge modes in a neon-xenon gas mixture at low pressure. *Plasma Sci. Tech.* **20**, 115401 (2018).
9. Abdelaziz Bouchikhi. Physical proprieties of DC glow discharges in a neon–argon gas mixture. *Can. J. Phys.* **96**, 62 (2018).
10. A. Bouchikhi. Nonlocal ionization theory and secondary electron emission coefficient: Application in helium and neon DC microdischarge at high pressure. *IEEE Trans. Plasma Science* **9**, 4260 (2019).
11. A. Bouchikhi. Modeling of a DC glow discharge in a neon–xenon gas mixture at low pressure and with metastable atom densities. *Plasma Sci. Tech.* **19**, 095403 (2017).

12. Y. Lin, R.A. Adomaitis. Simulation and model reduction methods for an RF plasma glow discharge. *J. Comp. Phys.* **171**, 731 (2001).

13. D. Loffhagen, M.M. Becker, A.K. Czerny, J. Philipp, C. Klages. Impact of hexamethyldisiloxane admixtures on the discharge characteristics of a dielectric barrier discharge in argon for thin film deposition. *Contrib. Plasma Phys.* **58**, 337 (2018).

14. S. Ponduri, M.M. Becker, S. Welzel, M.C.M. van de Sanden, D. Loffhagen, R. Engeln. Fluid modelling of CO_2 dissociation in a dielectric barrier discharge. *J. Appl. Phys.* **119**, 093301 (2016).

15. H. Hoft, M. Kettlitz, M.M. Becker, T. Hoder, D. Loffhagen, R. Brandenburg, K.-D. Weltmann. Breakdown characteristics in pulsed-driven dielectric barrier discharges: Influence of the pre-breakdown phase due to volume memory effects. *J. Phys. D: Appl. Phys.* **47**, 465206 (2014).

16. E. Eslami, A. Barjasteh, N. Morshedian. Numerical investigation of the effect of driving voltage pulse shapes on the characteristics of low-pressure argon dielectric barrier discharge. *Plasma Phys. Rep.* **41**, 519 (2015).

17. M. M. Becker, T. Hoder, R. Brandenburg, D. Loffhagen. Analysis of microdischarges in asymmetric dielectric barrier discharges in argon. *J. Phys. D: Appl. Phys.* **46**, 355203 (2013).

18. T. Samir, Y. Liu, L.-L. Zhao. Study on effect of neutral gas pressure on plasma characteristics in capacitive RF argon glow discharges at low pressure by fluid modeling. *IEEE Trans. Plasma Sci.* **46**, 1738 (2018).

19. Q. Liu, Y. Liu, T. Samir, Z. Ma. Numerical study of effect of secondary electron emission on discharge characteristics in low pressure capacitive RF argon discharge. *Phys. Plasmas* **21**, 083511 (2014).

20. M.M. Becker, H. Kählert, A. Sun, M. Bonitz, D. Loffhagen. Advanced fluid modeling and PIC/MCC simulations of low-pressure ccrf discharges. *Plasma Sources Sci. Tech.* **26**, 044001 (2017).

21. A. Barjasteh, E. Eslami. Numerical investigation of effect of driving voltage pulse on low pressure 90%Ar–10%Cl_2 dielectric barrier discharge. *Plasma Chem. Plasma Process* **38**, 261 (2018).

22. A. Barjasteh, E. Eslami, N. Morshedian. Experimental investigation and numerical modeling of the effect of voltage parameters on the characteristics of low-pressure argon dielectric barrier discharges. *Phys. of Plasmas* **22**, 073508 (2015).

23. N.B. Kolokolov, A.A. Kudrjavtsev, A.B. Blagoev. Interaction processes with creation of fast electrons in the low temperature plasma. *Phys. Scri.* **50**, 371 (1994).

24. E.W. Pike. On the mean lifetime of metastable neon atoms. *Phys. Rev.* **49**, 513 (1936).

25. G.J.M. Hagelaar, L.C. Pitchford. Solving the Boltzmann equation to obtain electron transport coefficients and rate coefficients for fluid models. *Plasma Sources Sci. Tech.* **14**, 722 (2005).

26. http://nl.lxcat.net/home/

27. L. Vriens, A.H.M. Smeets. Cross-section and rate formulas for electron-impact ionization, excitation, deexcitation, and total depopulation of excited atoms. *Phys. Rev. A* **22**, 940 (1980).

28. W.V. Gaens, A. Bogaerts. Kinetic modelling for an atmospheric pressure argon plasma jet in humid air. *J. Phys. D Appl. Phys.* **47**, 079502 (2014).

29. A. Bouchikhi, A. Hamid. 2D DC subnormal glow discharge in argon. *Plasma Sci. Tech.* **12**, 59 (2010).

30. A. Bouchikhi. Two-dimensional numerical simulation of the DC glow discharge in the normal mode and with Einstein's relation of electron diffusivity. *Plasma Sci. Tech.* **14**, 965 (2012).

31. G.J.M. Hagelaar, G.M.W. Kroesen, U. van Slooten, H. Schreuders. Modeling of the microdischarges in plasma addressed liquid crystal displays. *J. Appl. Phys.* **88**, 2252 (2000).

32. V.E. Golant, A.P. Zilinskij, I.E. Sacharov, S.C. Brown. *Fundamentals of Plasma Physics* (Wiley, 1980).

33. D.L. Scharfetter, H.K. Gummel. Large-signal analysis of a silicon read diode oscillator. *IEEE Trans. Elec. Dev.* **16**, 64 (1969).

34. A. Bouchikhi. Proposition of a new geometry of the electrodes in a particular discharge. *Indian J. Phys.* **94**, 353 (2020).

35. A. Bouchikhi. Parametric study on the DC microdischarge in a 90%helium–10%xenon gas mixture at intermediate pressure. *Indian J. Phys.* **96**, 1443 (2022).

36. L.S. Frost. Effect of Variable ionic mobility on ambipolar diffusion. *Phys. Rev.* **105**, 354 (1957).

37. Ph. Belenguer, J.P. Boeuf. Transition between different regimes of rf glow discharges. *Phys. Rev. A* **41**, 4447 (1990).

38. V. Lisovskiy, V. Yegorenkov, E. Artushenko, J-P. Booth, S. Martins, K. Landry, D. Douai, V. Cassagne. Normal regime of the weak-current mode of an rf capacitive discharge. *Plasma Sources Sci. Tech.* **22**, 015018 (2013).

39. S.K. Park, D.J. Economou. Parametric study of a radio-frequency glow discharge using a continuum model. *J. Appl. Phys.* **68**, 4888 (1990).

40. M. Meyyappan, T.R. Govindan. Radio frequency discharge modeling: Moment equations approach. *J. Appl. Phys.* **74**, 2250 (1993).

41. S.W. Hwang, H.-J. Lee, H.J. Lee. Effect of electron Monte Carlo collisions on a hybrid simulation of a low-pressure capacitively coupled plasma. *Plasma Sources Sci. Tech.* **23**, 065040 (2014).

42. M. Surendra, D. Vender. Collisionless electron heating by radio-frequency plasma sheaths. *Appl. Phys. Lett.* **65**, 153 (1994).

43. M. Surendra, D. Graves, L. Plano. Self consistent dc glow – discharge simulations applied to diamond film deposition reactors. *J. Appl. Phys.* **71**, 5189 (1992).

А. Боучіхі

ДОСЛІДЖЕННЯ РОЗРЯДУ
КРІЗЬ ДІЕЛЕКТРИЧНИЙ НЕОНОВИЙ БАР'ЄР
З ДЕЯКОЮ ГУСТИНОЮ МЕТАСТАБІЛЬНИХ
АТОМІВ ПРИ НИЗЬКОМУ ТИСКУ НА ЄМНІСНО
ЗАЛЕЖНІЙ РАДІОЧАСТОТІ: ВПЛИВ ТИСКУ

Досліджено розряд крізь діелектричний неоновий бар'єр з певною густиною метастабільних атомів на ємнісно залежній радіочастоті при тиску біля 4–12 Торр. Параметри транспорту у неоні залежать від енергії електронів в інтервалі 0,04–50 еВ. Використано одновимірну модель рідини і теорію дрейфу-дифузії для опису таких розрядів. В режимі усереднення по циклу розглянуто вплив тиску на властивості розрядів. Показано, що густини частинок, електричний потенціал та густина метастабільних атомів збільшуються з тиском. Також зростають концентрація поверхневого заряду і напруга на бар'єрному проміжку.

К л ю ч о в і с л о в а: ємнісно залежний, радіочастотний жевріючий розряд, закон Гауса, розряди крізь діелектричний бар'єр.